DEVELOPMENT OF A PHASE-AMPLITUDE COUPLING TOOLBOX FOR ASSESSING CHANGES IN CROSS-FREQUENCY COUPLING DUE TO DEEP BRAIN STIMULATION THERAPIES FOR TREATMENT RESISTANT DEPRESSION

A Thesis
Presented to
The Academic Faculty

by

Rehman Ali

In Partial Fulfillment
of the Requirements for the Degree
Bachelors of Science in the
School of Biomedical Engineering

Georgia Institute of Technology
May 2016

DEVELOPMENT OF A PHASE-AMPLITUDE COUPLING TOOLBOX FOR ASSESSING CHANGES IN CROSS-FREQUENCY COUPLING DUE TO DEEP BRAIN STIMULATION THERAPIES FOR TREATMENT RESISTANT DEPRESSION

Approved by:

Dr. Robert J. Butera, Advisor
School of Biomedical Engineering
Georgia Institute of Technology

Dr. Christopher J. Rozell
School of Electrical Engineering
Georgia Institute of Technology

Date Approved: April 29, 2016

ACKNOWLEDGEMENTS

I would like to thank my parents for their endless faith and support. I would also like to thank Mr. Tyrone Pannkuk, high school physics teacher and University Interscholastic League (UIL) Science coach at Ronald Reagan high school, for giving me the great opportunity to excel in math and science and guiding me on my way to become a great engineer. I would also like to thank graduate student advisor Vineet R. Tiruvadi (MD PhD candidate) for invaluable assistance with signal processing techniques, data interpretation, and both personal and professional development over the latter half of my undergraduate career.

TABLE OF CONTENTS

LIST OF FIGURES

LIST OF ABBREVIATIONS

MDD	Major Depressive Disorder
TRD	Treatment-Resistant Depression
TMS	Transcranial Magnetic Stimulation
ECT	Electroconvulsive Therapy
DBS	Deep Brain Stimulation
SCC	Subcallosal Cingulate
PET	Positron Emission Tomography
CFC	Cross-Frequency Coupling
CNS	Central Nervous System
PD	Parkinson's Disease
LFP	Local Field Potential
STN	Subthalamic Nucleus
EEG	Electroencephalography
ECoG	Electrocorticography
PAC	Phase Amplitude Coupling
PSD	Power Spectral Density
KL-MI	Kullback-Leibler-Based Modulation Index
HR	Heights Ratio
MVL-MI	Mean Vector Length Modulation Index
GLM	General Linear Model
PLV	Phase-Locking Value
CV	Coherence Value
MDD	Major Depressive Disorder

TRD	Treatment-Resistant Depression
PCA	Principal Component Analysis
CWT	Continuous Wavelet Transform
MSC	Magnitude-Squared Coherence
LS	Least Squares

LIST OF SYMBOL

A, $a_{HF}(t)$	High-frequency Amplitude
φ, $\varphi_{LF}(t)$	Low-frequency Phase
t	Continuous Time
n	Discrete Time Sample Index
f_s	Sampling Rate in Hz
A, B, C, D	Arbitrary Constants for Generic Phase Delayed Amplitude Modulation
f_{env}	Envelope Frequency
f_{car}	Carrier Frequency
$\epsilon(t)$	Gaussian Error Signal
φ	Phase Delay of the Low Frequency Oscillation
A_{env}, k, c, t_c, D	Arbitrary Constants For Sigmoidal Coupling
c, λ, A_{env}, D	Arbitrary Constants For Von Mises Coupling
s_1, s_2	Binomial Random Variables
k_1, k_2, c_1, c_2, t_{c1}, t_{c2}, A_{car0}, A_{env}	Arbitrary Constants For Biphasic Coupling
A_{car1}, A_{car2}	Carrier Amplitudes for Binomial Random Variables
$r_{decibel}$	Ripple on Decibel Scale
r_{linear}	Ripple on Linear Scale
$X_w(a, b)$	Continuous Wavelet Transform Output
a	Wavelet Scale Parameter
b	Time-Shift Parameter
$x(t)$	Input Signal to Continuous Wavelet Transform
$\psi(t)$	Mother Wavelet
F_b	Wavelet Bandwidth Parameter

F_c	Wavelet Center Frequency Parameter
$P(j)$	Normalized Discrete Distribution of Amplitude Binned by Phase
$Q(j)$	Arbitrary Discrete Distribution
N	Number of Phase Bins
j	Phase Bins Index
$D_{KL}(P, Q)$	Kullback-Leibler Divergence of $P(j)$ from $Q(j)$
$H(P)$	Shannon Entropy of $P(j)$
$U(j)$	Normalized Uniform Discrete Distribution
h_{min}	Minimum Normalized Amplitude Amongst Phase Bins
h_{max}	Maximum Normalized Amplitude Amongst Phase Bins
$\vec{a}_{HF}$	Column Vector for High-Frequency Amplitude Time Series
N	Number of Data Points in Time Series
$a_{HF_1} \dots a_{HF_N}$	Entries of $\vec{a}_{HF}$
$\varphi_{LF_1} \dots \varphi_{LF_N}$	Discrete Time Series of $\varphi_{LF}(t)$
$\epsilon_1 \dots \epsilon_N$	Discrete Time Series of $\epsilon(t)$
$\vec{\epsilon}$	Column Vector with Entries $\epsilon_1 \dots \epsilon_N$
X	Matrix for Least Squares Regression Problem
$\vec{\beta}$	Vector of Coefficients in Multiple Regression Problem
β_{cos}	Entry of $\vec{\beta}$ corresponding to cosine terms in X
β_{sin}	Entry of $\vec{\beta}$ corresponding to sine terms in X
β_o	Entry of $\vec{\beta}$ corresponding to column of ones in X
$\vec{\beta}_{LS}$	Least Squares Solution for $\vec{\beta}$
r_{GLM}	Correlation Coefficient in Multiple Regression Problem
z_{GLM}	Z-Score after Fisher Transformation of r_{GLM}

$\varphi_{HFA}(t)$	Phase of High-Frequency Amplitude Envelope
z_{PLV}	Z-Score after Arcsine Transformation of PLV
$a[n]$	Complex Amplitude Time-Series from $a_{HF_1} \ldots a_{HF_N}$, and $\varphi_{LF_1} \ldots \varphi_{LF_N}$
$\vec{a}[n]$	Time-Varying Vector from Real and Imaginary Parts of $a[n]$
σ_1^2, σ_2^2	Principal Variances of $\vec{a}[n]$
$\hat{u}_1, \hat{u}_2$	Orthogonal Unit Vectors in Principal Directions
$\vec{\mu}_a$	Mean Vector of $\vec{a}[n]$
θ	Angle that $\vec{\mu}_a$ makes with $\hat{u}_1$
$\sigma(\theta)$	Standard Deviation of $\vec{a}[n]$ in the $\vec{\mu}_a$ direction
z_{PCA}	Z-Score of $\vec{\mu}_a$
z_{CV}	Z-Score of Magnitude-Squared Coherence

SUMMARY

Phase-amplitude coupling (PAC) is theorized to play a fundamental physiological role in neuronal oscillations of the brain. This work contends that changes in PAC due to deep brain stimulation (DBS) in treatment-resistant depression (TRD) can account for the palliative effects observed in TRD patients. Part of this work compares the efficacy of six metrics for PAC based on their application to synthetic signals: the Kullback-Leibler-based modulation index (KL-MI), the heights ratio (HR), the general linear model (GLM), the phase locking value (PLV), the mean vector length normalized by principal component analysis (PCA), and the coherence value (CV). GLM gives the smallest region of detected coupling in the comodulograms, evades bimodality artifacts arising from the continuous wavelet transform (CWT) in this region of interest, and provides the greatest visual contrast. After an initial stage of validation and characterization of each metric, these metrics would then be applied to recorded local field potentials (LFP) before and after DBS to assess PAC. The goal of this work is to present a toolbox of metrics that are characterized on synthetic signals which would serve as a benchmark to clinicians for application to patient data.

CHAPTER 1

INTRODUCTION

Major depressive disorder (MDD) currently places large economic burdens on employers, health insurers, and the health care system (Simon et al., 2000). Treatment resistant depression (TRD), a subset of MDD, is associated with six-fold greater medical costs (around $30,000-40,000 per patient per year) as compared to non-TRD MDD patients, necessitating effective long-term treatment options for TRD (Crown et al., 2002). TRD currently lacks a universally-established definition and encompasses a highly heterogeneous patient population. Current metrics for evaluating TRD in patients include secondary assessments such as the inefficacy of at least two major treatments and scoring methods that give higher weight to more powerful treatments such as transcranial magnetic stimulation (TMS), electroconvulsive therapy (ECT) and deep brain stimulation (DBS) (McIntyre et al., 2014). The goal of our research group is to explore the mechanism by which DBS specifically treats TRD.

Research and clinical trials have isolated the subcallosal cingulate (SCC) as a possible source of excessive activity impacting multiple downstream effectors in the brain, which in part explains why diverse treatment options such as antidepressants, ECT, and TMS have been applied to MDD (Mayberg et al., 2005). In these trials, DBS has been shown to successfully suppress this overactivity through decreased glucose metabolism and blood flow as evaluated by positron emission tomography (PET) (Lozano et al., 2008). Research groups have also previously applied DBS to Parkinson's

disease to suppress similar hyperactivity in the basal ganglia (Fine et al., 2000, de Hemptinne et al., 2013).

Although the SCC has shown to be a promising therapeutic target for DBS in treatment of TRD, these same studies acknowledge a dearth of information regarding the mechanistic understanding of the effects of DBS at a neuronal level (Mayberg et al., 2005, Lozano et al., 2008). Innovative signal processing techniques that can elucidate this mechanism have been applied in pioneering work by Canolty et al. to explore cross-frequency coupling (CFC) between low frequency phase and high frequency amplitude in brain waves (Canolty et al., 2006). Various algorithms and statistics to evaluate and quantify CFC have been successfully applied by de Hemptinne et al. in developing a mechanistic understanding of the role of DBS in the alleviation of Parkinson's disease symptoms (de Hemptinne et al., 2013). We hope to use similar approaches in elucidating the role of DBS in TRD.

By developing an understanding of how DBS of the SCC alters CFC in TRD, we can get closer to a cellular mechanism by which DBS affects the SCC and how this therapeutic target exerts its effects on other region involved in TRD. Assessing this CFC in neuronal oscillations from TRD patients necessitates the creation of a signal processing toolbox that would enable the clinician to diagnose and monitor TRD.

Detecting Cross-Frequency Coupling

Cross-Frequency Coupling (CFC) within brain waves has the potential to elucidate the mechanism behind neural disorders of the central nervous system (CNS) which has previously been shown in the case of Parkinson's disease (PD) (de Hemptinne et al., 2013). Typically, this process involves assessing the effects of deep brain

stimulation (DBS) on a therapeutic target (generally a well-established effector of the disorder) by looking at CFC in recorded local field potentials (LFPs) at various locations around brain (Canolty and Knight, 2010). There are various forms of CFC such as phase-phase, phase-amplitude, and amplitude-amplitude. LFPs are generally governed by the inverse-square law, which dictates how signal strength coming from a current source decays with distance; therefore, multiple LFP readings are taken at various locations around a region of the brain in hopes of isolating the latent sources of neuronal activity (Buzsaki et al., 2012). De Hemptinne et al. apply DBS to the subthalamic nuclei (STN) to assess consequent changes in CFC in the motor cortex after demonstrating significant differences between PD and other neurological disorders such as other forms of dystonia and epilepsy (de Hemptinne et al., 2013). In the case of treatment resistant depression (TRD), various studies have previously established the subcallosal cingulate (SCC) as a locus of metabolic hyperactivity as assessed by positron emission tomography (PET), and clinical trials involving DBS have confirmed the aforementioned findings (Mayberg et al., 2005, Lozano et al., 2008). We hope to understand how DBS of the SCC alters CFC in TRD through various LFPs recorded using electroencephalography (EEG) and electrocorticography (ECoG).

Currently, phase-amplitude coupling (PAC) is currently the most examined form of CFC due to empirical evidence of its existence and relevance (Canolty and Knight, 2010). Low-frequency phase is theorized to modulate high-frequency amplitude because low frequency brain waves act over larger temporal and spatial scales than high frequency brain waves. The idea is that small groups of neurons in high frequency oscillations are activated along the phase of a larger low frequency oscillation which can

reveal physiological roles (Canolty and Knight, 2010, Buzsaki et al., 2012). Thus, PAC can be measured between the phase of a low-frequency oscillation and the amplitude of a high-frequency oscillation. A physiological interpretation of this behavior would be that a region of the brain operating at some low-frequency oscillation plays a role in modulating the high-frequency activity at another location in the brain (Canolty and Knight, 2010) such as between the subthalamic nucleus and the motor cortex in Parkinson's Disease (de Hemptinne et al., 2013). Contrary to intuition, power spectral density (PSD) estimation does not capture changes in PAC because PAC is intended to detect correlational relationships between phases and amplitudes between low-frequency and high-frequency bands rather than synchronous changes in signal power at two frequencies.

Band-Pass Filtering Considerations

Assessment of phase-amplitude CFC generally involves band-pass filtering the brain wave signal around the two frequencies in question and analyzing low-frequency phase modulation of high-frequency amplitude. Hilbert transforms applied to the band-pass-filtered signal extract phase and amplitude information within those bands. Important considerations must be taken in band-pass filtering design. For example, if the pass-band is too narrow, the amplitude modulation characteristics of the signal at a certain frequency may be lost, precluding any further analysis (Aru et al., 2014). On the other hand, if a band-pass filter is too wide, information at other frequencies may drown out time-domain information at the frequency being analyzed or diminish the resolution of detected PAC in frequency for amplitude.

Berman et al. suggest that the most efficient approach to band-pass filtering is to set the bandwidth to be at least two times the low frequency that the high frequency

oscillation would be coupled to (Berman et al., 2012). However, as the frequency-for-phase increases, CFC will have less resolution in frequency-for-amplitude. Regardless, this variable-bandwidth approach avoids false-negatives that would otherwise arise when using a fixed-bandwidth approach.

Metrics for Detecting Phase-Amplitude Coupling

There are various metrics for assessing PAC (Canolty and Knight, 2010, Tort et al., 2010): the Kullback-Leibler-based modulation index (KL-MI), the heights ratio (HR), the mean vector length modulation index (MVL-MI), the general linear model (GLM), the phase locking value (PLV), and the coherence value (CV). The MVL-MI, established by Canolty et al., involves creating a complex-valued ($Ae^{i\varphi}$) time-series from high-frequency amplitude (A) low-frequency phase (φ). This complex-valued time-series can be expressed as a time-varying vector in the complex plane, and the mean-vector is the average of the time-series. Thus, in theory, if there were no coupling between the amplitude and phase, the mean vector length would be close to zero, but if coupling were present, the mean vector would have a significantly large magnitude.

The flaw with simply taking the mean vector length (MVL) as the MI is that scaling the amplitude would scale the mean vector, but this would measure power rather than coupling (Cohen, 2014). To help deal with this scaling invariance, surrogates are generated by randomly shifting the amplitude along the phase, and a z-score is assigned to the original MVL, which is calculated based on the normal distribution of the MVL of the surrogates (Canolty et al., 2006). However, this solution only works for measuring transient coupling. In order to measure stationary coupling, it may still be possible to establish statistical significance based on the original distribution of the $Ae^{i\varphi}$ time-series

in the complex plane alone. This motivates the application of principal component analysis (PCA) in the complex plane to assign statistical significance to the MVL for measuring stationary coupling. One goal of this work is to demonstrate the efficacy of PCA against five well-established metrics for PAC: KL-MI, HR, GLM, PLV, and CV. We are interested in determining which method better demonstrates the CFC as it may guide future research in the area because these metrics are widely used on patient data. However, the characterization of these metrics through synthetic signals is ongoing (Tort et al., 2010). Continued work would help to better contextualize the results of these metrics on patient data. Furthermore, it is important to not only provide the clinician with a PAC toolbox, but also a thorough characterization of its tools.

CHAPTER 2

METHODOLOGY

The synthetic signals below exhibit PAC and are modeled in continuous time t. For the discrete time implementation of these signals, $t = n/f_s$, where f_s is the sampling rate, and n is discrete time. In this work, f_s is fixed to 1024.599795 Hz, and each synthetic signal is 10000 samples long. This synthetic data is an input to one of two band-pass filtering algorithms which isolate the oscillations at various frequency bands of interest. The amplitude and phase of these oscillations are then extracted and applied as inputs to various PAC metrics to compare their performances under each band-pass filtering algorithm. A heat map called a comodulogram is generated by analyzing multiple frequencies for phase and frequencies for amplitude at once.

Generating Synthetic Data

Generic phase-delayed amplitude modulation

The most basic synthetic signal for testing metrics for PAC is phase-delayed amplitude modulation (Tort et al., 2010). The general form for this signal is

$$x_{AM}(t) = \big(A + Bcos(2\pi f_{env}t)\big)cos(2\pi f_{car}t) + Ccos(2\pi f_{env}t - \varphi) + D\epsilon(t) \quad (1)$$

where A, B, C, and D are constants, φ is the phase delay of the low frequency oscillation, f_{env} is the envelope frequency, f_{car} is the carrier frequency, and $\epsilon(t)$ is standard Gaussian white noise (standard deviation of one and mean of zero). In this setup, PAC is

expected between f_{env}, the frequency for phase, and f_{car}, the frequency for amplitude. For our synthetic signal we assigned the following values: A = 1.2, B = 1.1, C = 0.4, D = 0.3, f_{env} = 4 Hz, f_{car} = 60 Hz, and $\varphi = \pi/4$

Sigmoidal coupling

One form of nonlinear coupling is sigmoidal coupling (Penny et al., 2008). The general form for a synthetic signal with sigmoidal coupling is

$$x_{SG}(t) = \frac{k}{1+\exp(-c(A_{env}cos(2\pi f_{env}t-\varphi)-t_c)}cos(2\pi f_{car}t) +$$

$$A_{env}cos(2\pi f_{env}t - \varphi) + D\epsilon(t) \qquad (2)$$

where k, c, t_c, A_{env}, and D are constants, φ is phase delay, f_{env} is the envelope frequency, f_{car} is the carrier frequency, and $\epsilon(t)$ is standard white noise. PAC is expected between f_{env}, and f_{car}. For the sigmoidal coupling synthetic signal, we assigned the following values: k = 2, c = 1, t_c = – 0.95, $A_{env,}$ = 1, D = 1, f_{env} = 6 Hz, f_{car} = 35 Hz, and $\varphi = \pi/4$.

Von Mises coupling

Another form of nonlinear coupling is Von Mises coupling (Penny et al., 2008). The general form for a synthetic signal with Von Mises coupling is

$$x_{VM}(t) = \frac{c}{\exp(\lambda)}\exp(\lambda\cos(2\pi f_{env}t - \varphi))\, cos(2\pi f_{car}t)$$

$$+A_{env}cos(2\pi f_{env}t - \varphi) + D\epsilon(t) \qquad (3)$$

where c, λ, A_{env}, and D are constants, φ is phase delay, f_{env} is the envelope frequency, f_{car} is the carrier frequency, and $\epsilon(t)$ is standard white noise. PAC is expected between f_{env}, and f_{car}. For the sigmoidal coupling synthetic signal, we assigned the following values: $c = 1$, $\lambda = 0.95$, $A_{env,} = 1$, $D = 1.5$, $f_{env} = 9$ Hz, $f_{car} = 50$ Hz, and $\varphi = \pi/4$.

Biphasic coupling

Biphasic coupling take two sigmoidal nonlinearities and adds them together in a stochastic way. The following set of equations demonstrate how biphasic coupling occurs:

$$A_{car1} = \frac{k_1}{1+\exp(-c_1(A_{env}cos(2\pi f_{env}t-\varphi)-t_{c1})}$$

$$A_{car2} = \frac{k_2}{1+\exp(-c_2(A_{env}cos(2\pi f_{env}t-\varphi)-t_{c2})} \quad (4)$$

$$x_{VM}(t) = (s_1A_{car1} + s_2A_{car2} + A_{car0})cos(2\pi f_{car}t)$$

$$+ A_{env}cos(2\pi f_{env}t - \varphi) + D\epsilon(t) \quad (5)$$

In this case, s_1 and s_2 are independent and distinct binomial random variable whose values can be 0 or 1 with a 50% probability. For the biphasic coupling synthetic signal, we assigned the following values: $k_1 = 8$, $k_2 = 4$, $c_1 = -10$, $c_2 = 10$, $t_{c1} = 0.95$, $t_{c2} = -0.95$, $A_{car0} = 2$, $A_{env} = 1$, $D = 1$, $f_{env} = 11$ Hz, $f_{car} = 70$ Hz, and $\varphi = \pi/4$.

Band-Pass Filtering Approaches

Variable-bandwidth band-pass filtering

Chebyshev type I digital band-pass filters with pass-band ripples of 2% (linear scale) were used to filter the synthetic signals. This filter was chosen because of its quick initial roll-off from the passband while keeping the pass-band ripple relatively small (2%). The following conversion was used to convert linear scale ripple r_{linear} to decibel scale ripple $r_{decibel}$:

$$r_{decibel} = 40 \log_{10} \left(\frac{1+r_{linear}}{1-r_{linear}} \right) \quad (6)$$

When filtering for low-frequency phase, the bandwidth was fixed to 2 Hz. Thus, a single band-pass filtered signal will correspond to a single low-frequency phase analyzed. However, in order to obtain the modulating envelope over a high-frequency oscillation, the bandwidth was set to 2.4 times the low-frequency phase for which PAC was being tested. Thus, for a single high-frequency at which amplitude modulation occurs, there are multiple band-pass filtered signals for each low-frequency phase analyzed.

Continuous wavelet transform with complex Morlet

The continuous wavelet transform (CWT) can be evaluated as the inner product below

$$X_w(a,b) = \frac{1}{|a|^{1/2}} \int_{-\infty}^{\infty} x(t) \psi^* \left(\frac{t-b}{a} \right) dt \quad (7)$$

where $\psi(t)$ is the mother wavelet, * denotes complex conjugate, a is the wavelet scale, and b is the time-shift parameter. The mother wavelet applied in our analyses was the complex Morlet whose form is

$$\psi(t) = \frac{1}{\sqrt{\pi F_b}} e^{-t^2/F_b} e^{-i2\pi F_c t} \quad (8)$$

where F_b and F_c are the bandwidth parameter and wavelet center frequency parameters respectively (Misiti, 2007). Equation (7) may be reinterpreted as a convolution in the case of a Morlet wavelet due to the fact that $\psi^*\left(\frac{t-b}{a}\right) = \psi\left(\frac{b-t}{a}\right)$:

$$X_w(a,b) = \frac{1}{|a|^{1/2}} \int_{-\infty}^{\infty} x(t)\psi\left(\frac{b-t}{a}\right) dt \quad (9)$$

The wavelet convolution in equation (19) corresponds to multiplication in the frequency domain by a Gaussian-shaped band-pass filter around the center frequency. Furthermore, wavelets are generally constant-Q, i.e., they have a constant bandwidth to center frequency ratio (Vetterli and Herley, 1992). Therefore, for any selection of F_b and F_c, the bandwidth of the resulting Gaussian band-pass filter increases with center frequency. Lastly, the center frequency f_c is inversely related to the wavelet scale a by F_c ($a = F_c/f_c$). Thus, the continuous wavelet transform of the synthetic signal was calculated for scales corresponding to both the low frequencies for phase and the high frequencies for amplitude. In this work, we chose the following parameter values for the complex Morlet: $F_b = 1$, and $F_c = 1$.

Additional transformations to band-pass filtered data

A signal coming from variable-bandwidth band-pass filtering has to be Hilbert-transformed. A signal coming from the continuous wavelet transform already comes as an analytic signal because of our use of the complex Morlet. The absolute value of the analytic signal yields the envelope from which the high-frequency amplitude modulation

may be assessed. The complex argument of the analytic signal yields the phase angle from which the low-frequency phase may be assessed.

Phase-amplitude coupling metrics

Kullback-Leibler-based modulation index

The algorithm of the KL-MI (Tort et al., 2010) begins by binning high-frequency amplitude into low-frequency phase. We chose to use 36 phase bins over 360° such that bin 1 collects high-frequency amplitudes that occur when low-frequency phase is from 0° to 10°. Bin 2 does the same from 10° to 20°, etc. The amplitude values in each bin *j* is averaged to produce a histogram of high-frequency amplitude versus low-frequency phase. This histogram is then normalized by dividing each bin by the sum of all the bins to produce a discrete distribution *P*(*j*). The Kullback-Leibler divergence of *P*(*j*) from an arbitrary distribution *Q*(*j*) over N total bins (our N = 36) is as follows:

$$D_{KL}(P,Q) = \sum_{j=1}^{N} P(j) \ln \frac{P(j)}{Q(j)} \tag{10}$$

The definition of the Shannon entropy of *P*(*j*) is the following:

$$H(P) = -\sum_{j=1}^{N} P(j) \ln P(j) \tag{11}$$

The Shannon entropy simplifies the Kullback-Leibler divergence of *P*(*j*) from the uniform distribution *U*(*j*) (a value of 1/N over N bins) to the following:

$$D_{KL}(P,U) = \ln N - H(P) \tag{12}$$

The Kullback-Leibler divergence of $P(j)$ from $U(j)$ is then normalized by $\ln N$ to obtain the KL-MI which is zero if $P(j) = U(j)$ and unity if the distribution of $P(j)$ resembles a Kronecker delta:

$$MI = \frac{D_{KL}(P,U)}{\ln N} = \frac{\ln N - H(P)}{\ln N} = 1 - \frac{H(P)}{\ln N} \quad (13)$$

A KL-MI of zero corresponds to no measurable PAC and a KL-MI closer to one would correspond to a significant PAC.

Heights ratio

The HR is based on the same histograms used for KL-MI; however, instead of calculating a Kullback-Leibler divergence, the maximum amplitude (h_{max}) and the minimum amplitude (h_{min}) amongst the bins are used to make a ratio that represents the strength of coupling. Lakatos et al. define this ratio to be h_{max}/h_{min} (Lakatos et al., 2005), and Tort et al. use $(h_{max} - h_{min})/h_{max}$ (Tort et al., 2010). However, for the purposes of following conventions used by AM radio (Tort et al., 2010), we define HR as $(h_{max} - h_{min})/(h_{max} + h_{min})$.

General linear model

To determine GLM, PAC is determine through correlational methods involving the phase $\varphi_{LF}(t)$ at low frequencies, and amplitude envelope $a_{HF}(t)$ at high frequencies. The following matrix equation represents the multiple regression problem for GLM (Penny et al., 2008):

$$\vec{a}_{HF} = \begin{bmatrix} a_{HF_1} \\ \vdots \\ a_{HF_N} \end{bmatrix} = \begin{bmatrix} \cos(\varphi_{LF_1}) & \sin(\varphi_{LF_1}) & 1 \\ \vdots & \vdots & \vdots \\ \cos(\varphi_{LF_N}) & \sin(\varphi_{LF_N}) & 1 \end{bmatrix} \begin{bmatrix} \beta_{cos} \\ \beta_{sin} \\ \beta_o \end{bmatrix} + \begin{bmatrix} \epsilon_1 \\ \vdots \\ \epsilon_N \end{bmatrix} = X\vec{\beta} + \vec{\epsilon} \quad (14)$$

where $\vec{a}_{HF}$ is a column vector whose entries are the discrete time series of $a_{HF}(t)$, $[\varphi_{LF_1} \ldots \varphi_{LF_N}]$ is the discrete time series of $\varphi_{LF}(t)$, $\vec{\beta}$ is a vector of coefficients in the multiple regression problem, and $\vec{\epsilon}$ is a vector of residuals. Because (14) an over-constrained system, only a least squares solution (LS) can be obtained for $\vec{\beta}$:

$$\vec{\beta}_{LS} = (X^T X)^{-1} X^T \vec{a}_{HF} \quad (15)$$

The residual error vector $\vec{\epsilon}$ can then be calculated as the following:

$$\vec{\epsilon} = \vec{a}_{HF} - X\vec{\beta}_{LS} \quad (16)$$

The r^2_{GLM} value for this multiple regression equation may be calculated as the following:

$$r^2_{GLM} = \frac{\vec{a}_{HF} \cdot \vec{a}_{HF} - \vec{\epsilon} \cdot \vec{\epsilon}}{\vec{a}_{HF} \cdot \vec{a}_{HF}} \quad (17)$$

A Fisher transformation is performed on the resulting r_{GLM} to obtain the following z-score z_{GLM} which is the output GLM metric for PAC:

$$z_{GLM} = \tanh^{-1} r_{GLM} \quad (18)$$

Phase-locking value

The high-frequency amplitude is added to its Hilbert transform times the imaginary unit *i* to obtain its analytic signal. Phase $\varphi_{HFA}(t)$ is extracted from the high-frequency amplitude (HFA) by taking the complex argument of its analytic signal. The

following equation is the PLV (Lachaux et al., 1999) between $\varphi_{HFA}(t)$ and $\varphi_{LF}(t)$ for PAC (Vanhatalo et al., 2004, Mormann et al., 2005):

$$PLV = \frac{1}{N}\sum_{n=1}^{N} \exp(i(\varphi_{HFA}[n] - \varphi_{LF}[n])) \tag{19}$$

This PLV is arcsine transformed to obtain a z-score z_{PLV} which is the PAC metric from PLV:

$$z_{PLV} = \sin^{-1}(2PLV - 1) \tag{20}$$

Mean vector z-score based on principal component analysis

The low frequency phase $\varphi_{LF}[n]$ and the high frequency amplitude $a_{HF}[n]$ time-series are used to construct the following time-varying complex-valued phasor (Canolty et al., 2006, Canolty and Knight, 2010):

$$a[n] = a_{HF}[n]e^{i\varphi_{LF}[n]} = Re\{a[n]\} + i\, Im\{a[n]\} \tag{21}$$

A two-dimensional column vector $\vec{a}[n]$ is constructed from $Re\{a[n]\}$ and $Im\{a[n]\}$:

$$\vec{a}[n] = \begin{bmatrix} Re\{a[n]\} \\ Im\{a[n]\} \end{bmatrix} \tag{22}$$

The covariance matrix $COV[\vec{a}]$ is calculated from $\vec{a}[n]$, and its matrix diagonalization is the following:

$$COV[\vec{z}] = [\hat{u}_1 \quad \hat{u}_2] \begin{bmatrix} \sigma_1^2 & 0 \\ 0 & \sigma_2^2 \end{bmatrix} \begin{bmatrix} \hat{u}_1 \\ \hat{u}_2 \end{bmatrix} \tag{23}$$

where σ_1^2 and σ_2^2 are the principal variances of $\vec{a}[n]$ in the $\hat{u}_1$ and $\hat{u}_2$ directions, which form the principal axes. This particular eigen-decomposition is also known as principal component analysis (PCA).

We denote $\vec{\mu}_a$ as the mean vector of $\vec{a}[n]$. Because $\hat{u}_1$ and $\hat{u}_2$ form an orthonormal basis, projections of $\vec{\mu}_a$ onto the principal axes are simplified by dot products. Our goal is to find the standard deviation of $\vec{a}[n]$ in the direction of $\vec{\mu}_a$. We can determine the angle θ that $\vec{\mu}_a$ makes with the first principal axis through the following equation:

$$\theta = \cos^{-1}\left(\frac{\vec{\mu}_a \cdot \hat{u}_1}{\|\vec{\mu}_a\|}\right) = \cos^{-1}\left(\frac{\vec{\mu}_a \cdot \hat{u}_1}{\sqrt{\vec{\mu}_a \cdot \vec{\mu}_a}}\right) \tag{24}$$

PCA assumes that there is an ellipse that represents the standard deviation of $\vec{a}[n]$ in all directions. This standard deviation σ as a function of θ is as follows:

$$\sigma(\theta) = \sqrt{(\sigma_1 \cos\theta)^2 + (\sigma_2 \sin\theta)^2} \tag{25}$$

The $\sigma(\theta)$ function (25) is evaluated at the value of θ from equation (24) to obtain the standard deviation in the direction of $\vec{\mu}_a$. The z-score z_{PCA} can be calculated from $\vec{\mu}_a$ and $\sigma(\theta)$ as $z_{PCA} = \|\vec{\mu}_a\|/\sigma(\theta) = \left(\sqrt{\vec{\mu}_a \cdot \vec{\mu}_a}\right)/\sigma(\theta)$. Conceptually, by taking the ratio of the mean vector length to the standard deviation in the direction of the mean vector, the distance of the mean vector from the origin has been normalized. This is meaningful because z_{PCA} is invariant to scaling, which means that it measures PAC rather than variations in power across frequency bands. This mean vector z-score is the PCA-based metric for PAC (**Figure 1**).

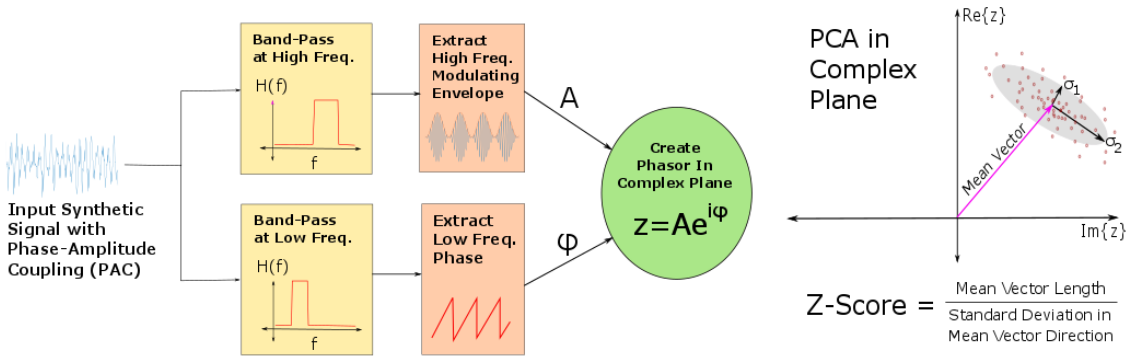

Figure 1. General Schematic for Mean Vector Length Z-Score by PCA. This new application of PCA involves normalization of mean vector length in the complex plane by standard deviation in the direction of the mean vector. This normalization ensures the scaling invariance of the metric and isolates PAC from amplitude-amplitude coupling.

Coherence Value

CV takes the magnitude-squared coherence (MSC) between the high-frequency amplitude oscillation and the original signal of interest before any band-pass filtering (Colgin et al., 2009). The z-score z_{CV} is determined by taking the Fisher transformation of the aforementioned MSC ($z_{CV} = \tanh^{-1} MSC$) (Jirsa and Muller, 2013). This z-score is the PAC metric based on CV.

The major advantage of this method is that for a fixed high frequency for amplitude, multiple low frequencies for phase can be examined at once. The process of extracting high frequency amplitude by the CWT is unaffected by this. However, the bandwidth of the Chebyshev type I band-pass filter used to obtain the high-frequency amplitude is changed from being variable to being fixed at 2.4 times the highest frequency for phase being examined.

Because increasing the bandwidth also increases the uncertainty in the frequency for amplitude at which PAC is occurring, CV gives more precise information regarding

the frequency for amplitude at which PAC occurs when the frequency for phase is lower. As a result, this last metric works very well once a small range for the frequency for phase has been isolated by inspecting PAC by one of the five primary metrics above (KL-MI, HR, GLM, PLV, and PCA). Thus, CV should be used as a secondary confirmation metric for PAC.

CHAPTER 3

RESULTS

Each of the five primary metrics (KL-MI, HR, GLM, PLV, and PCA) give consistent results for phase-delayed amplitude modulation after variable-bandwidth band-pass filtering (**Figure 1**). There is significant PAC around the 4 Hz frequency for phase and 60 Hz frequency for amplitude in each comodulogram. Although the region of detected coupling is relatively small and triangle-shaped for variable-bandwidth band-pass filtering, this region after the CWT (**Figure 2**) is a large smeared box. This box is smeared towards high frequency for amplitude and high frequency for phase due to their constant bandwidth-to-center frequency ratio (Vetterli and Herley, 1992). GLM, followed by KL-MI and PCA, tend to confine this smearing to a smaller range of frequencies for phase. Lastly, CV is shown to give the smallest region of coupling in both frequency for phase and frequency for amplitude after variable-bandwidth band-pass filtering (**Figure 2**). This is not the case for frequency for amplitude after CWT (**Figure 3**) due to the aforementioned smearing. Note, however, that CV is most effective once a small region for frequency for phase and frequency for amplitude has been identified.

PAC seems to be dulled in the region of interest for sigmoidal coupling (6 Hz frequency for phase and 35 Hz frequency for amplitude) (**Figures 4 and 5**) and biphasic coupling (11 Hz frequency for phase and 70 Hz frequency for amplitude) (**Figures 8 and 9**). GLM, followed by PLV and PCA, provide the best contrast amongst primary metrics after variable-bandwidth band-pass filtering. GLM, followed by KL-MI and PCA, seem to provide the best contrast amongst primary metrics after the CWT. CV is able to confine a smaller region for frequency for phase and frequency for amplitude for sigmoidal coupling after both variable-bandwidth band-pass filtering and the CWT. This is not the case for biphasic coupling.

Von Mises coupling shows the best-behaved comodulograms (**Figures 6 and 7**) regardless of the band-pass filtering approach used. They all show coupling around 9 Hz frequency for phase and 50 Hz frequency for amplitude as expected.

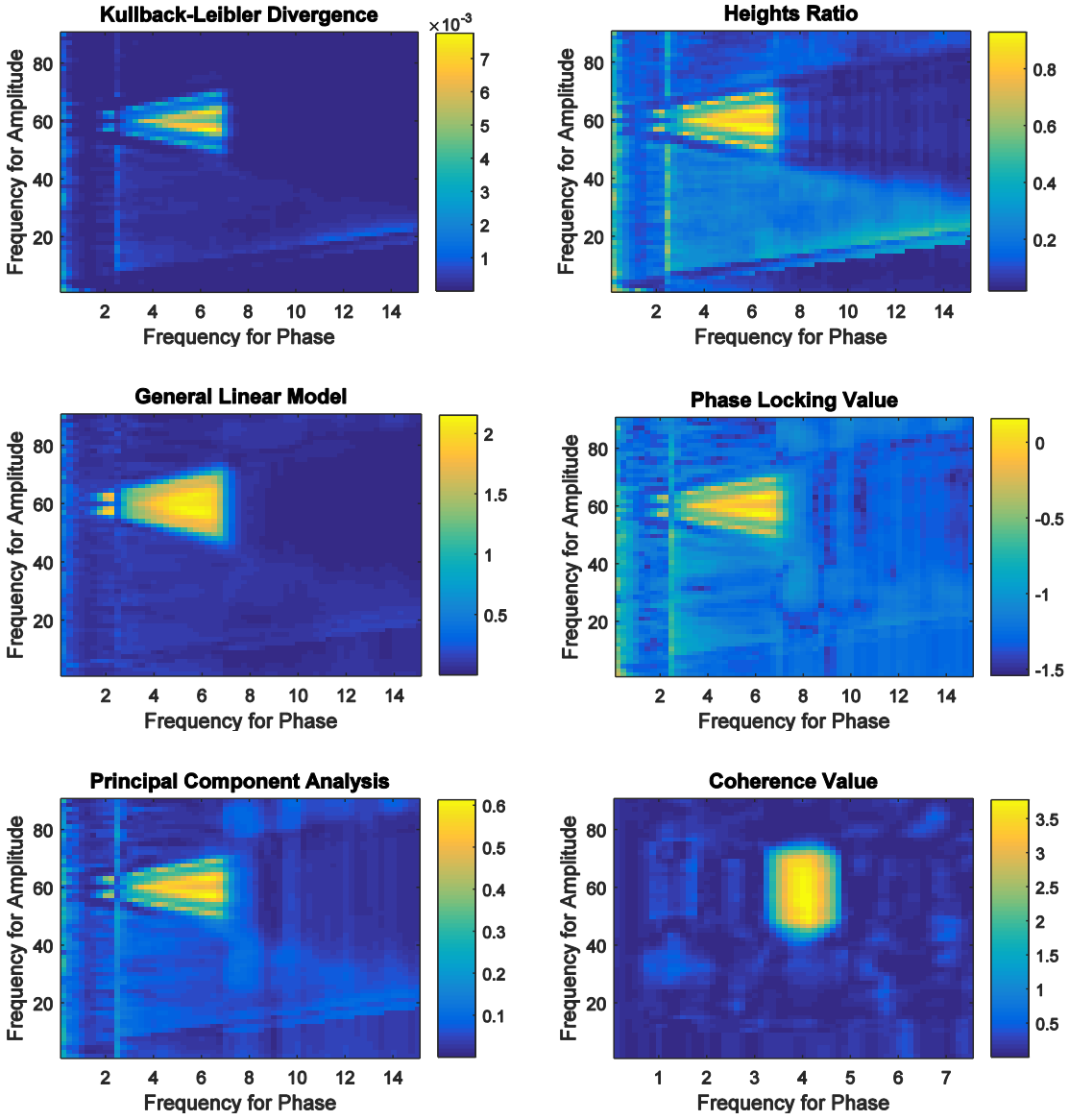

Figure 2. Comodulograms for Generic Phase-Delayed Amplitude Modulation. Frequency for amplitude and frequency for phase were extracted by variable-bandwidth band-pass filtering. Results are shown for Kullback-Leibler divergence (KL-MI), heights ratio (HR), general linear model (GLM), phase-locking value (PLV), principal component analysis (PCA), and coherence value (CV).

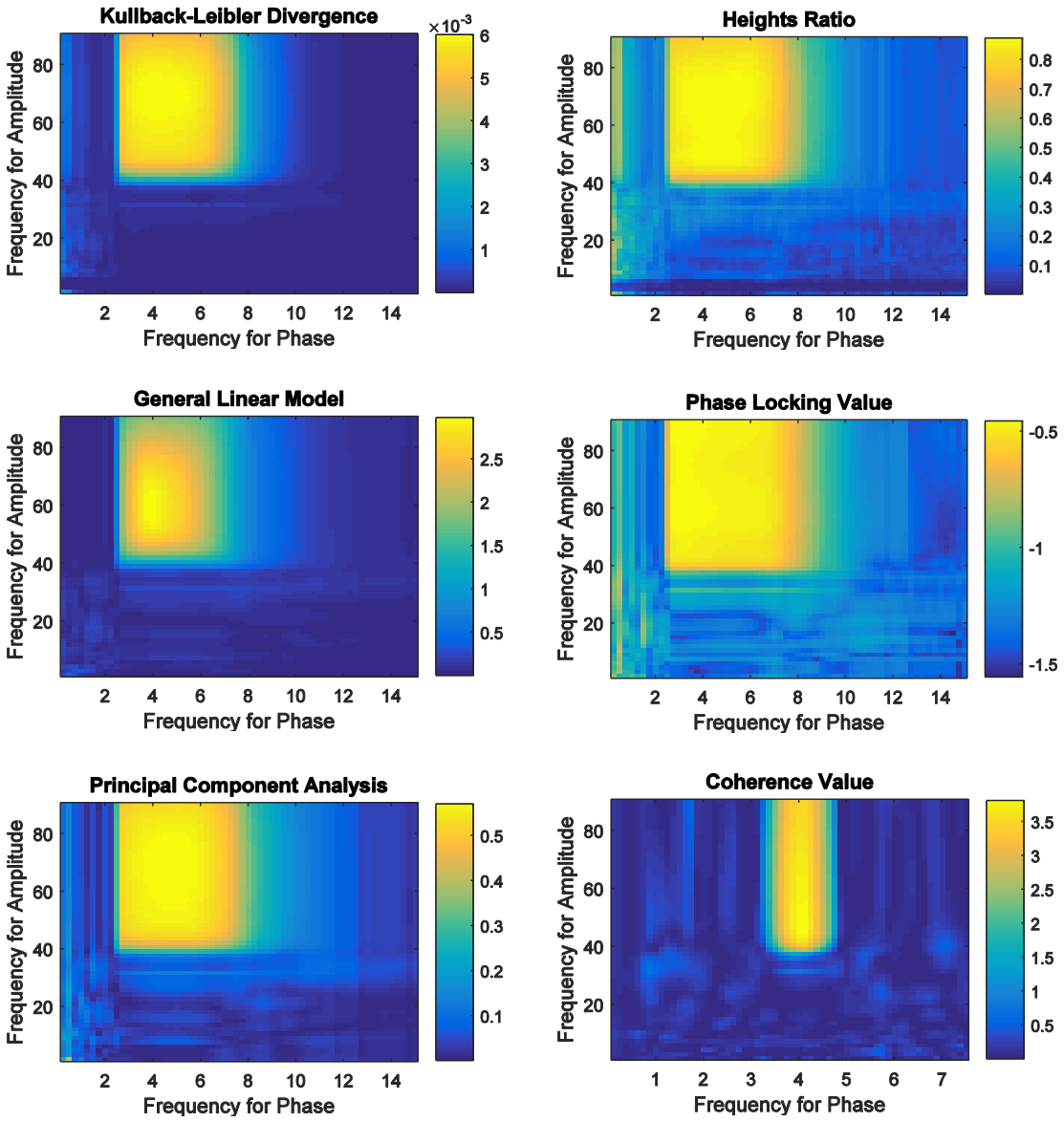

Figure 3. Comodulograms for Generic Phase-Delayed Amplitude Modulation. Frequency for amplitude and frequency for phase were extracted by the continuous wavelet transform (CWT) with the complex Morlet. Results are shown for Kullback-Leibler divergence (KL-MI), heights ratio (HR), general linear model (GLM), phase-locking value (PLV), principal component analysis (PCA), and coherence value (CV).

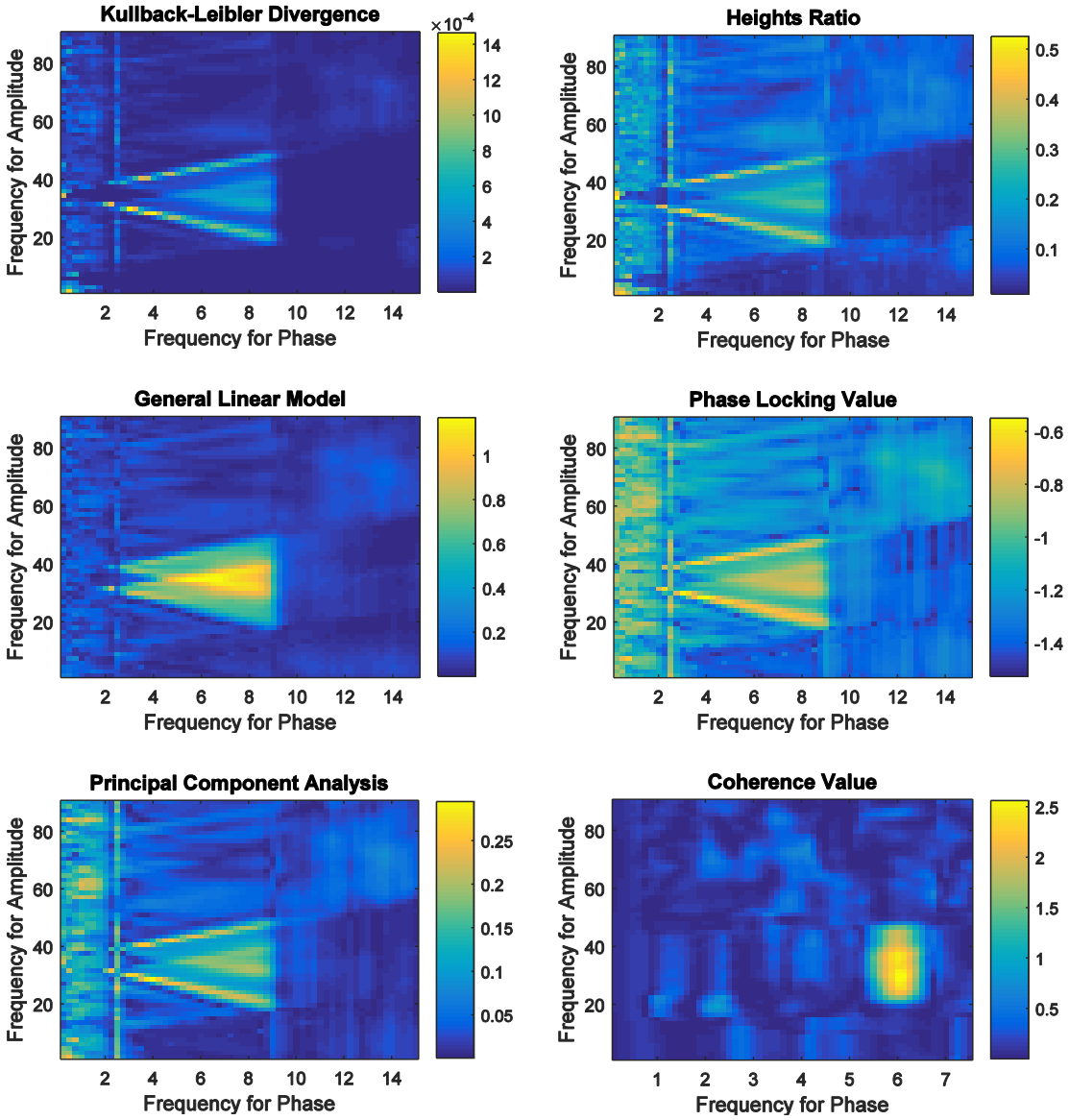

Figure 4. Comodulograms for Sigmoidal Coupling. Frequency for amplitude and frequency for phase were extracted by variable-bandwidth band-pass filtering. Results are shown for Kullback-Leibler divergence (KL-MI), heights ratio (HR), general linear model (GLM), phase-locking value (PLV), principal component analysis (PCA), and coherence value (CV).

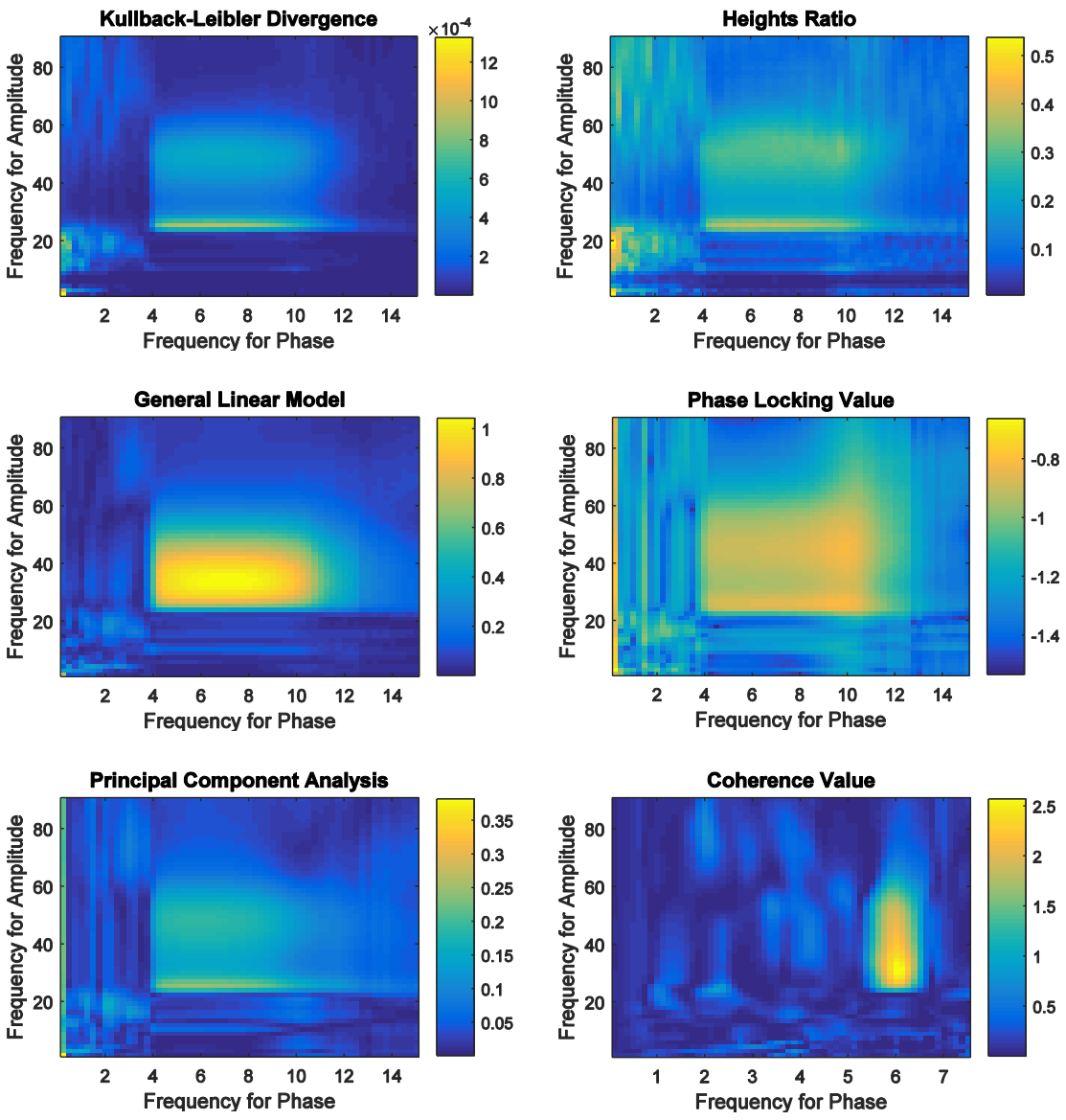

Figure 5. Comodulograms for Sigmoidal Coupling. Frequency for amplitude and frequency for phase were extracted by the continuous wavelet transform (CWT) with the complex Morlet. Results are shown for Kullback-Leibler divergence (KL-MI), heights ratio (HR), general linear model (GLM), phase-locking value (PLV), principal component analysis (PCA), and coherence value (CV).

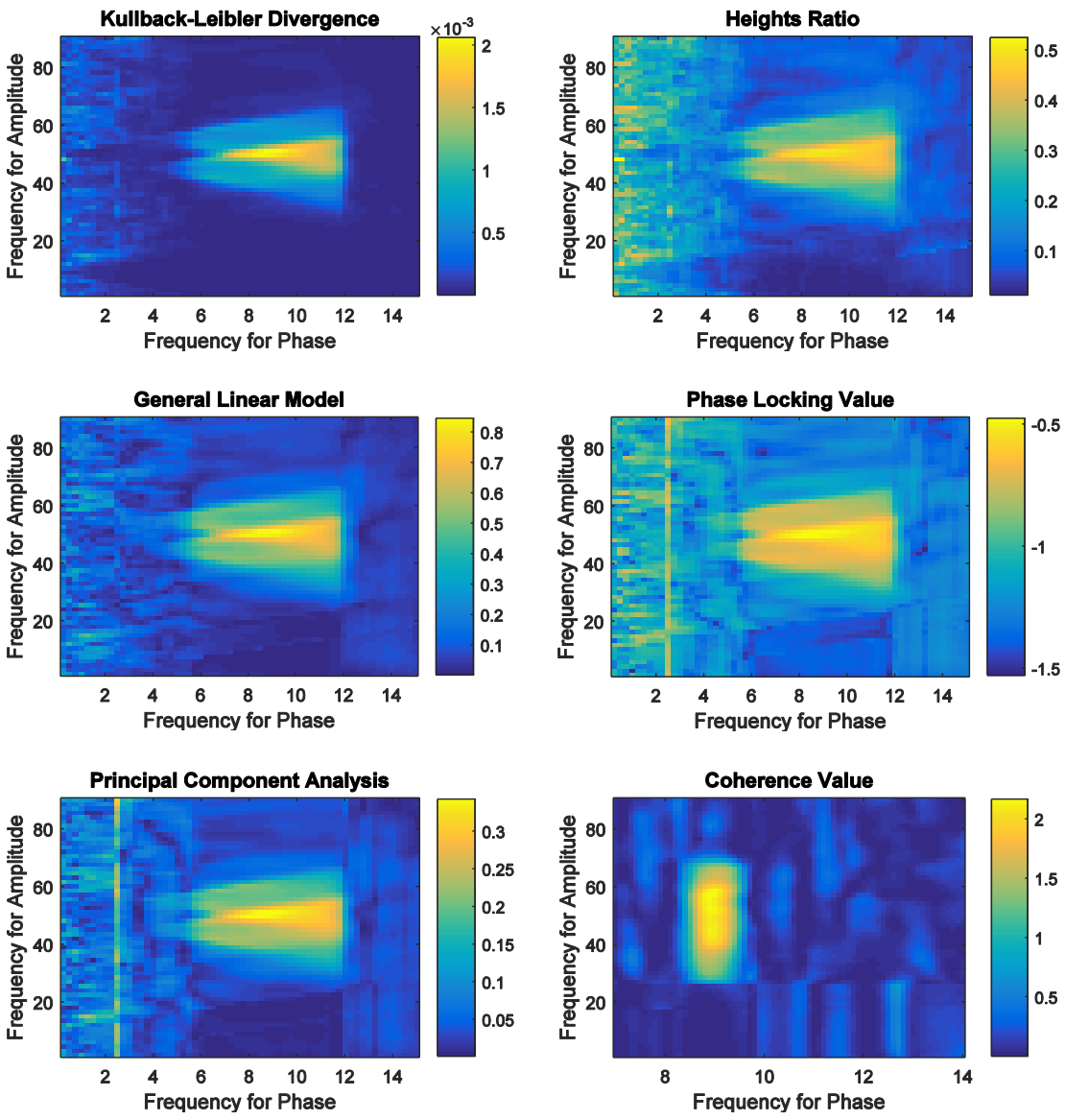

Figure 6. Comodulograms for Von Mises Coupling. Frequency for amplitude and frequency for phase were extracted by variable-bandwidth band-pass filtering. Results are shown for Kullback-Leibler divergence (KL-MI), heights ratio (HR), general linear model (GLM), phase-locking value (PLV), principal component analysis (PCA), and coherence value (CV).

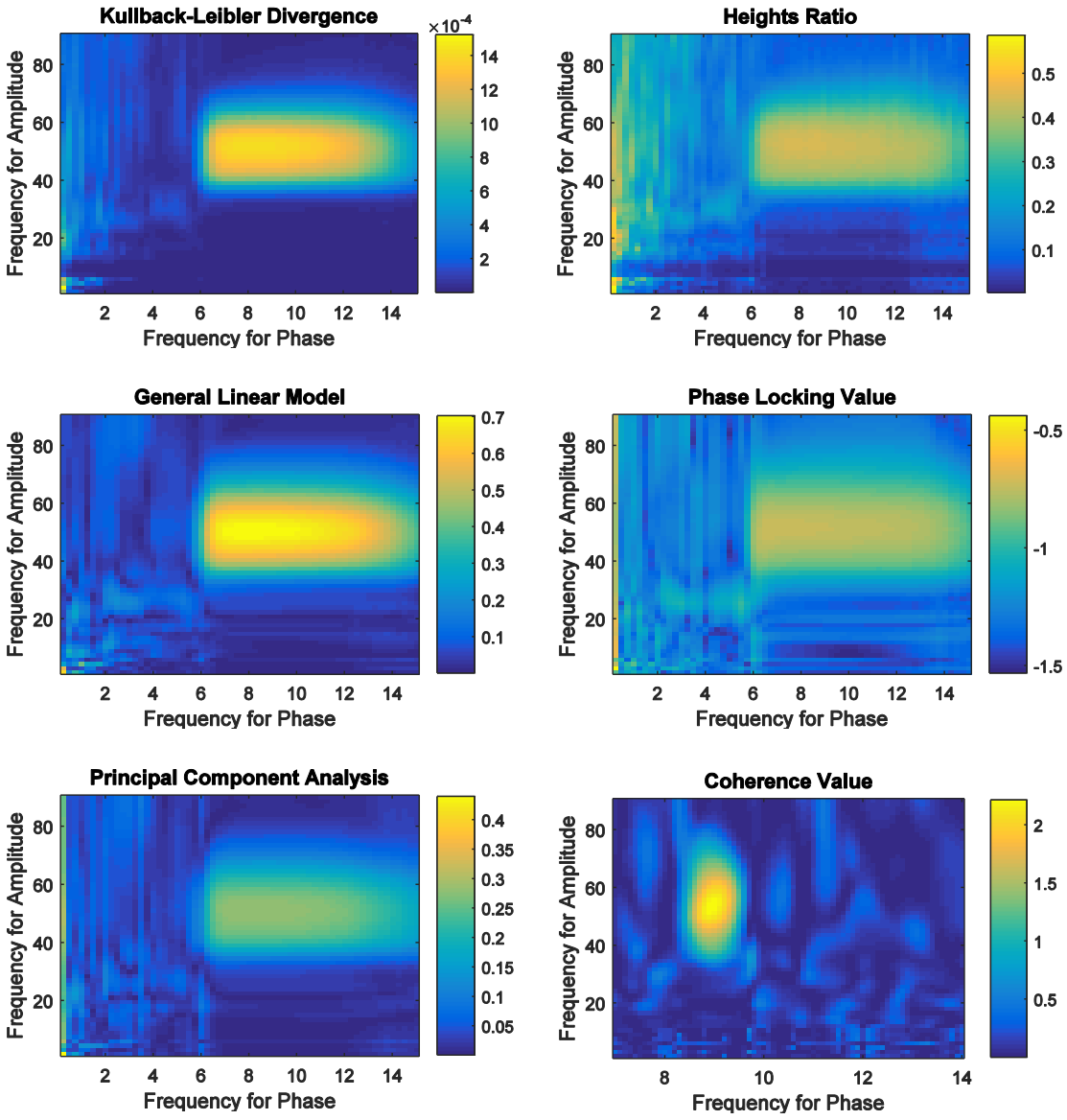

Figure 7. Comodulograms for Von Mises Coupling. Frequency for amplitude and frequency for phase were extracted by the continuous wavelet transform (CWT) with the complex Morlet. Results are shown for Kullback-Leibler divergence (KL-MI), heights ratio (HR), general linear model (GLM), phase-locking value (PLV), principal component analysis (PCA), and coherence value (CV).

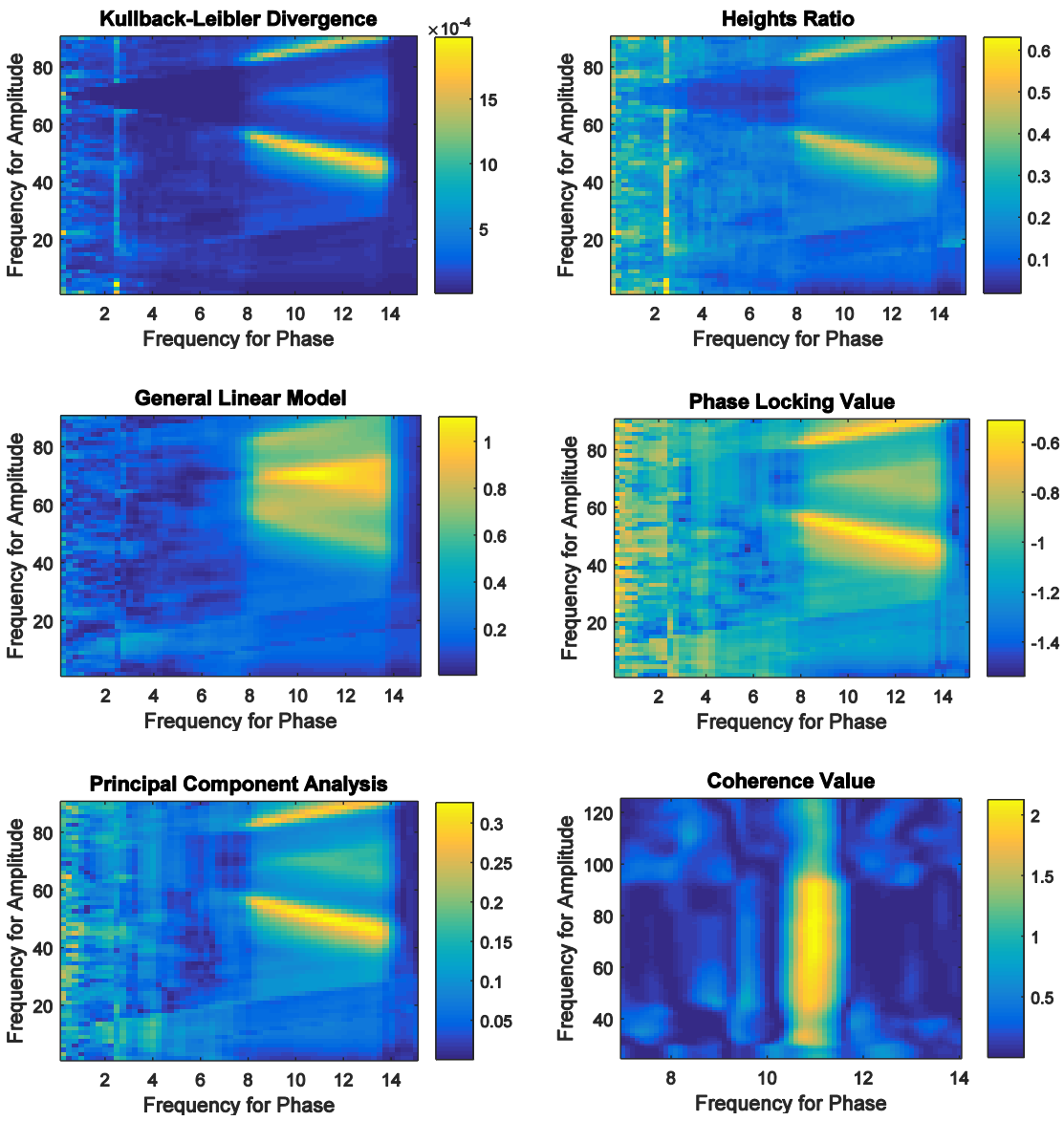

Figure 8. Comodulograms for Biphasic Coupling. Frequency for amplitude and frequency for phase were extracted by variable-bandwidth band-pass filtering. Results are shown for Kullback-Leibler divergence (KL-MI), heights ratio (HR), general linear model (GLM), phase-locking value (PLV), principal component analysis (PCA), and coherence value (CV).

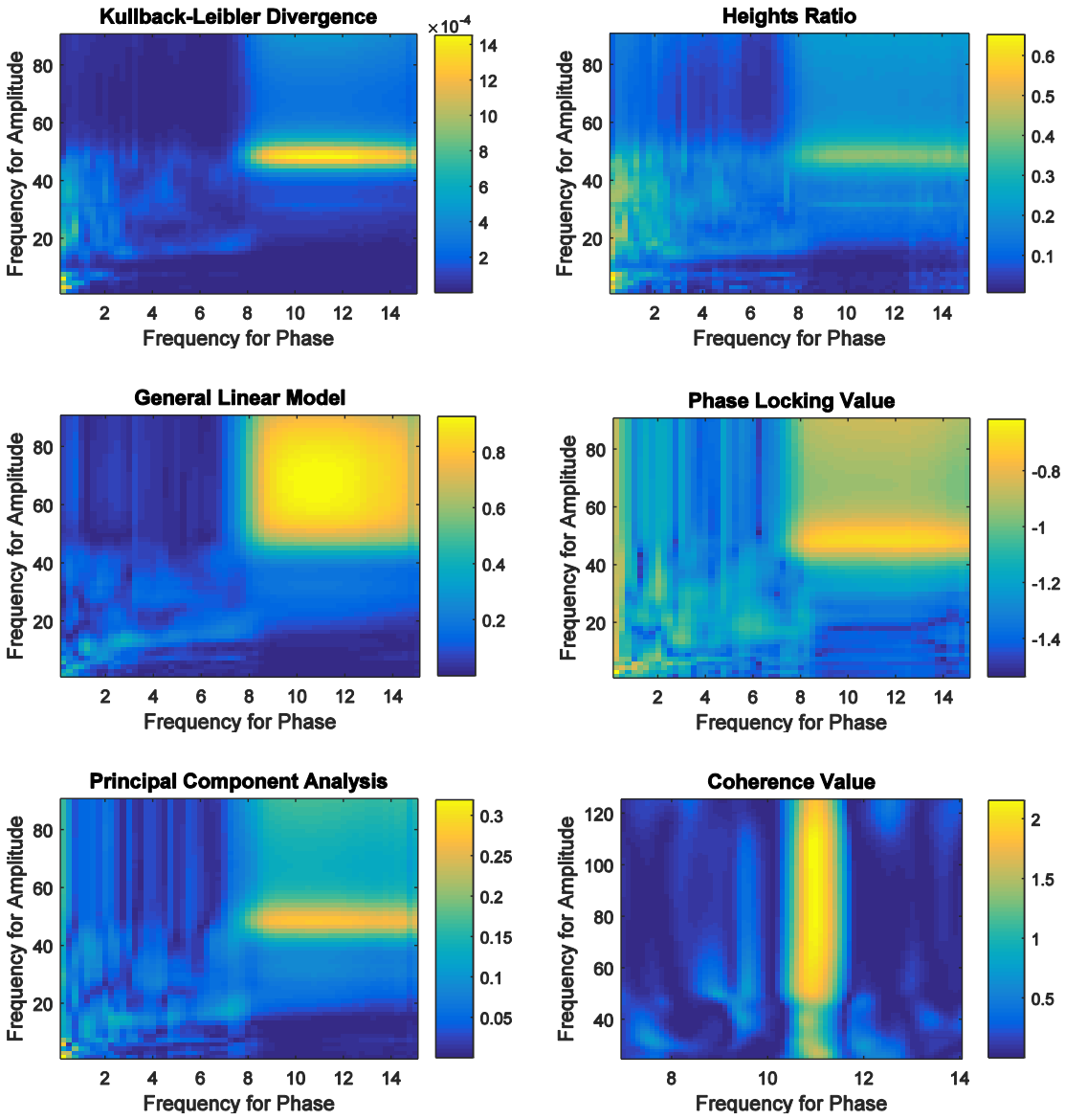

Figure 9. Comodulograms for Biphasic Coupling. Frequency for amplitude and frequency for phase were extracted by the continuous wavelet transform (CWT) with the complex Morlet. Results are shown for Kullback-Leibler divergence (KL-MI), heights ratio (HR), general linear model (GLM), phase-locking value (PLV), principal component analysis (PCA), and coherence value (CV).

CHAPTER 4

DISCUSSION

There are some important tradeoffs arising from the variable-bandwidth band-pass filter. As the frequency for phase increases, the resolution in frequency for amplitude decreases (Berman et al., 2012). Although the comodulogram provides more precise regions for PAC at lower frequencies for phase, the uncertainty principle between the time domain and frequency domain begins to take effect. At lower frequencies, larger epochs of time are needed in order to evaluate PAC. However, this would significantly increase the length of signal recording and computation time. Thus, results may inaccurately or erroneously indicate PAC for very low frequencies for phase. However, for the band-pass filter arising from the complex Morlet, the resolution in frequency for amplitude depends on the frequency for amplitude rather than the frequency for phase.

The general trend when moving from variable-bandwidth band-pass filtering to the CWT is increased smearing towards higher frequencies. Furthermore, in some cases, the band-pass filter from CWT produces a bimodal region with respect to frequencies for amplitude (**Figures 5 and 9**). The unequal attenuation of sidebands around the frequency for amplitude due to the Gaussian shape of this band-pass filter causes two separate regions to arise in comodulogram. One of these regions will be at a frequency for amplitude lower that the expected frequency for phase because of unequal attenuations at the lower sideband and the carrier frequency. This will indicate a frequency for amplitude between the carrier frequency and the lower sideband frequency. The second region will be at a higher frequency for amplitude between the carrier frequency and upper sideband

frequency for similar reasons. Additionally, this second region at the higher frequency is smeared out with respect to frequency for amplitude because of the same general trend for smearing at higher frequencies.

One technique to decrease this bimodality artifact in a comodulogram is to increase the bandwidth of the complex Morlet by increasing F_b. However, increasing the bandwidth decreases the resolution of the comodulogram by smearing the frequency for amplitude. Therefore, this tradeoff between bimodality artifacts and resolution is a terminal limitation of applying the CWT with the complex Morlet.

In addition to the bimodality artifact mentioned above, there is a trimodality (Fig. 7) artifact that can be observed after variable-bandwidth band-pass filtering. This trimodality artifact arises because of nonlinearities present in the modulating envelope over the carrier frequency. In theory, there should be a multimodal distribution in the frequency for amplitude due to these nonlinearities, but the broadband Gaussian noise added to the signal hides these additional spectral sidebands.

Amongst all primary metrics used, the GLM consistently proves to be the most effective metric in almost every regard. For each synthetic signal and each band-pass filtering technique (**Figures 2-9**), the GLM gives a relatively small region of detected coupling with strong contrast against surrounding regions. Furthermore, the comodulograms generated by GLM after the CWT (Figs. 4 and 8) do not show any bimodality artifacts as opposed to other primary metrics.

All metrics showed PAC around the appropriate frequency for phase and frequency for amplitude pair. Even though the PCA approach does not stand out against the other metrics applied here, the results show that PCA is a reliable way of evaluating

PAC when compared to the other metrics. These results were significant because although PCA does not improve the performance of PAC detection, PCA enables detection of stationary coupling by using the complex time-varying vector approach implemented by Canolty et al (Canolty et al., 2006, Canolty and Knight, 2010). As a result, the complex time-varying vector approach can be used to address transient and stationary coupling in exploratory PAC, extending its applications.

CHAPTER 5

CONCLUSIONS AND FUTURE WORK

The testing of metrics on synthetic data is a significant contribution to computational neuroscience because the characterization of each metric in terms of its strengths, limitations, and tradeoffs, ultimately guides the interpretation of patient data in the future. A major implication of this work is that now a new class of metrics based on PCA has been introduced to the family of PAC metrics, which needs to be better characterized for use in the future.

Future work needs to address improvements in band-pass filtering techniques that will improve detection of PAC by these metrics. Further investigation into why regions in the comodulograms are shaped as they are (triangular vs. square, etc.), and explanations for other observed artifacts are still lacking. The long term implications of these method would be real-time comodolography of recorded signals from the brain. As such, the low-level optimization of algorithms based on hardware architecture for real-time signal processing applications (Dellavale et al.) needs to be addressed. All of the metrics and band-pass filtering considerations discussed here also need to be examined for real-time applications. Such a real-time system would greatly facilitate the detection of PAC within and across brain waves in a clinical research setting.

Finally, the most important questions to address are the practical implementation of these algorithms on LFPs (Aru et al., 2014). Some forms of PAC are task-dependent (i.e. transient) while others are long term (stationary). The type of PAC depends strongly on the experimental setup and the nature of the activity being measured. These

considerations greatly impact epoch length when analyzing LFPs. If the nature of this transience changes as the experiment progresses, an adaptive element may be necessary in determining the appropriate epoch length and analysis windows for signals being inputted to these algorithms. All of these considerations must be taken into account when deciding when and how to apply the new PCA approach introduced in this paper. No metric in particular provides complete information regarding PAC (Canolty and Knight, 2010, Tort et al., 2010); thus, it is important to understand the limitations of each metric and to examine PAC from every angle possible.

REFERENCES

Buzsaki G, Anastassiou CA, Koch C (2012) The origin of extracellular fields and currents - EEG, ECoG, LFP and spikes. Nat Rev Neurosci 13:407-420.

Canolty RT, Edwards E, Dalal SS, Soltani M, Nagarajan SS, Kirsch HE, Berger MS, Barbaro NM, Knight RT (2006) High gamma power is phase-locked to theta oscillations in human neocortex. Science 313:1626-1628.

Canolty RT, Knight RT (2010) The functional role of cross-frequency coupling. Trends in cognitive sciences 14:506-515.

Colgin LL, Denninger T, Fyhn M, Hafting T, Bonnevie T, Jensen O, Moser MB, Moser EI (2009) Frequency of gamma oscillations routes flow of information in the hippocampus. Nature 462:353-357.

Crown WH, Finkelstein S, Berndt ER, Ling D, Poret AW, Rush AJ, Russell JM (2002) The impact of treatment-resistant depression on health care utilization and costs. J Clin Psychiat 63:963-971.

de Hemptinne C, Ryapolova-Webb ES, Air EL, Garcia PA, Miller KJ, Ojemann JG, Ostrem JL, Galifianakis NB, Starr PA (2013) Exaggerated phase-amplitude coupling in the primary motor cortex in Parkinson disease. Proc Natl Acad Sci U S A 110:4780-4785.

Fine J, Duff J, Chen R, Hutchison W, Lozano AM, Lang AE (2000) Long-Term Follow-up of Unilateral Pallidotomy in Advanced Parkinson's Disease. New England Journal of Medicine 342:1708-1714.

Jirsa V, Muller V (2013) Cross-frequency coupling in real and virtual brain networks. Frontiers in computational neuroscience 7:78.

Lachaux JP, Rodriguez E, Martinerie J, Varela FJ (1999) Measuring phase synchrony in brain signals. Human brain mapping 8:194-208.

Lakatos P, Shah AS, Knuth KH, Ulbert I, Karmos G, Schroeder CE (2005) An oscillatory hierarchy controlling neuronal excitability and stimulus processing in the auditory cortex. Journal of neurophysiology 94:1904-1911.

Lozano AM, Mayberg HS, Giacobbe P, Hamani C, Craddock RC, Kennedy SH (2008) Subcallosal cingulate gyrus deep brain stimulation for treatment-resistant depression. Biological psychiatry 64:461-467.

Mayberg HS, Lozano AM, Voon V, McNeely HE, Seminowicz D, Hamani C, Schwalb JM, Kennedy SH (2005) Deep brain stimulation for treatment-resistant depression. Neuron 45:651-660.

McIntyre RS, Filteau MJ, Martin L, Patry S, Carvalho A, Cha DS, Barakat M, Miguelez M (2014) Treatment-resistant depression: definitions, review of the evidence, and algorithmic approach. Journal of affective disorders 156:1-7.

Misiti M (2007) Wavelets and their applications. London ; Newport Beach, CA: ISTE.

Mormann F, Fell J, Axmacher N, Weber B, Lehnertz K, Elger CE, Fernandez G (2005) Phase/amplitude reset and theta-gamma interaction in the human medial temporal lobe during a continuous word recognition memory task. Hippocampus 15:890-900.

Penny WD, Duzel E, Miller KJ, Ojemann JG (2008) Testing for nested oscillation. J Neurosci Meth 174:50-61.

Simon GE, Revicki D, Heiligenstein J, Grothaus L, VonKorff M, Katon WJ, Hylan TR (2000) Recovery from depression, work productivity, and health care costs among primary care patients. General Hospital Psychiatry 22:153-162.

Tort AB, Komorowski R, Eichenbaum H, Kopell N (2010) Measuring phase-amplitude coupling between neuronal oscillations of different frequencies. Journal of neurophysiology 104:1195-1210.

Vanhatalo S, Palva JM, Holmes MD, Miller JW, Voipio J, Kaila K (2004) Infraslow oscillations modulate excitability and interictal epileptic activity in the human cortex during sleep. Proc Natl Acad Sci U S A 101:5053-5057.

Vetterli M, Herley C (1992) Wavelets and filter banks: theory and design. Signal Processing, IEEE Transactions on 40:2207-2232.

VITA

REHMAN ALI

ALI was born in Philadelphia, Pennsylvania. He attended Ronald Reagan high school in San Antonio, Texas before moving to Atlanta, Georgia to attend the Georgia Institute of Technology. While in San Antonio, he was the team captain of the UIL Science team and a two-time state finalist. During his senior year, he assembled a UIL Science team that reached the state finals. He also won the State AP Scholar award which goes to one male and one female in each state based on the number of AP exams passed. He will receive a B.S. in Biomedical Engineering with minors in Chemistry and Spanish from Georgia Institute of Technology in May 2016. During his time at Georgia Institute of Technology, he was the recipient of the Henry Ford II Scholar award which is administered by the College of Engineering to the best student at the end of the third year in the Biomedical Engineering department. He is currently a differential equations teaching assistant. His plans immediately after graduation are to obtain an MS in Electrical Engineering with a concentration on Signal Processing. His career goals are to become a leading MD PhD in the area of human physiological signal processing. When he is not working on his research, Mr. Ali enjoys helping others, volunteering at clinics, toying with electronics, discussing politics, and watching Spanish television.